Pharmaceutical Research, Vol. 26, No. 12, December 2009 (© 2009)
DOI: 10.1007/s11095-009-9975-2

Research Paper

Long- and Short-Range Electrostatic Interactions Affect the Rheology of Highly Concentrated Antibody Solutions

Ravi Chari,[1] Kavita Jerath,[1] Advait V. Badkar,[2] and Devendra S. Kalonia[1,3]

Received June 3, 2009; accepted September 14, 2009; published online October 1, 2009

Purpose. To explain the differences in protein-protein interactions (PPI) of concentrated *versus* dilute formulations of a model antibody.
Methods. High frequency rheological measurements from pH 3.0 to 12.0 quantitated viscoelasticity and PPI at high concentrations. Dynamic light scattering (DLS) characterized PPI in dilute solutions.
Results. For concentrated solutions at low ionic strength, the storage modulus, a viscosity component and a measure of PPI, is highest at the isoelectric point (pH 9.0) and lowest at pH 5.4. This profile flattens at higher ionic strength but not completely, indicating PPI consist of long-range electrostatics and other short-range attractions. At low concentrations, PPI are near zero at pI but become repulsive as the pH is shifted. Higher salt concentrations completely flatten this profile to zero, indicating that these PPI are mainly electrostatic.
Conclusions. This discrepancy occurs because long-range interactions are significant at low concentrations, whereas both long- and short-range interactions are significant at higher concentrations. Computer modeling was used to calculate antibody properties responsible for long- and short-range interactions, i.e. net charge and dipole moment. Charge-charge interactions are repulsive while dipole-dipole interactions are attractive. Their net effect correlated with the storage modulus profile. However, only charge-charge repulsions correlated with PPI determined by DLS.

KEY WORDS: computer modeling; dipole; highly concentrated protein solutions; protein-protein interactions; viscosity.

INTRODUCTION

As the active ingredient in therapeutic liquid formulations or as observed within physiological systems, proteins are often highly concentrated or exist in a crowded state (1,2). A highly concentrated solution has greater than 10% of its volume occupied by solute (1,2). In contrast, a crowded solution refers to a highly concentrated solution whose solutes consist of the protein of interest as well as co-solutes (1,2). In this case, the protein may occupy less than 10% of the solution volume, but the effects of preferential exclusion due to the co-solutes cause the protein molecules to sequester, resulting in localized regions where the protein is highly concentrated (3). The more concentrated or crowded a solution, the smaller the average distance among protein solute molecules and the greater the frequency of encounter and the duration of interaction among them. For a liquid protein formulation such as that of a therapeutic monoclonal antibody (mAb), these increased protein-protein interactions (PPI) result from the drug's manufacture at high concentrations. Such a constraint is necessary to ensure delivery of the active ingredient at the appropriate dose in as little volume as possible (4,5). This is especially important for subcutaneous injections, which are typically limited to 1.5 mL or less (6). Unfortunately, PPI in such formulations can affect properties such as viscosity and may increase the probability of aggregation, a process in which proteins partially unfold and irreversibly combine to form non-functional higher order complexes (7,8). Formulations with high viscosity are substantially more difficult to prepare and administer (5,6,9) while the increased rate of aggregation decreases drug shelf-life (5). Loss of potency, changes in pharmacokinetic profile, and compromised product safety are also concerns. With regard to physiological systems, certain conditions and diseases have been found to result partly from PPI that manifest in the formation and deposition of aggregate protein

Electronic supplementary material The online version of this article (doi:10.1007/s11095-009-9975-2) contains supplementary material, which is available to authorized users.

[1] Department of Pharmaceutical Sciences, School of Pharmacy, University of Connecticut, 69 North Eagleville Rd., U-3092, Storrs, Connecticut 06269, USA.
[2] Global Biologics, Pfizer Global Research and Development, Chesterfield, Missouri 63017, USA.
[3] To whom correspondence should be addressed. (e-mail: kalonia@uconn.edu)

ABBREVIATIONS: B_{22}, second osmotic virial coefficient; B'_{22}, second osmotic virial coefficient multiplied by solute molecular weight; CD, circular dichroism; DLS, dynamic light scattering; E_{B22}, pairwise energetic interaction term; G', storage modulus of complex viscosity; G'', loss modulus of complex viscosity; IgG, immunoglobulin G; k_D, interaction parameter from DLS; mAb, monoclonal antibody; $|\eta^*|$, magnitude of complex viscosity; PDB, Protein Databank; PPI, protein-protein interaction(s); V_{B22}, excluded volume term.

complexes within the body. Examples include ocular conditions such as eye cataracts (10); neurological diseases such as familial amyloid polyneuropathy, and Alzheimer's, Parkinson's, and Huntington's diseases (11,12); and kidney disorders such as light-chain deposition disease and myeloma cast nephropathy (13,14).

To address these concerns, an understanding of PPI in concentrated solutions is needed. This would aid in establishing the solution conditions under which the protein remains most stable and where formulation viscosity does not hinder handling. Techniques such as static and dynamic light scattering involve analyzing dilute protein solutions and assuming the results to be applicable at higher concentrations. The former gives the osmotic second virial coefficient (B_{22}), a thermodynamic measure of the solution's deviation from ideality (15). The latter yields the interaction parameter (k_D), which is a function of B_{22} and protein hydrodynamics (16). Both properties are measures of PPI at low concentrations. They are used to determine the conditions in which a protein remains soluble as well as those that lead to crystallization or precipitation (17). The interactions that cause protein association in the latter case(s) may also eventually result in aggregation (8). This suggests a link between B_{22} and k_D and long-term protein stability. However, such findings may not always be applicable to highly concentrated formulations, since those properties are determined under dilute conditions.

Fortunately, a high-frequency shear rheometer recently developed in our laboratory allows for the direct analysis of highly concentrated solutions (18–20). Samples are subjected to an oscillatory stress applied at megahertz frequencies, and solution viscoelastic properties are obtained. These include the complex viscosity ($|\eta^*|$), storage modulus (G'), and loss modulus (G''). All three are positive and have a minimum value of zero. G' is a measure of the energy stored in the solution under stress while G'' quantitates energy dissipated during oscillation. In particular, G' was determined to be an ideal parameter for quantitating PPI, especially at high concentrations (20). At low concentrations (<40 mg/ml), it is not significantly different from that of water. The theory behind the technique and the derivation of the moduli are included in the online Supplementary Materials (21).

We have previously shown that PPI within a solution of a model IgG2 mAb differ at high *versus* low concentrations (20). At 120 mg/ml, G' decreased from pH 4.0 to 5.4 then increased as the pH was raised to the mAb's pI of 9.0. This means that at high concentrations protein-protein attractions decreased from pH 4.0 to 5.4 and then increased until pH 9.0. In contrast, both the B_{22} and k_D from light scattering studies simply decreased from pH 4.0 to 9.0. In other words, at relatively low concentrations, the PPI were marked by straightforward decreasing repulsions and/or increasing attractions across that pH range. Furthermore, the mAb solution was opalescent at the pI at high concentrations but became clear upon dilution. Apparently, protein association occurs at high concentrations, but reverses when the concentration is lowered. This suggests that the PPI governing that process are strongly attractive, but weaken sharply when the solution is diluted (22). In fact, the attractions are mitigated to the point that both B_{22} and k_D are near zero at the pI (22).

The above findings establish that PPI observed at high concentrations do not always correlate with those determined under dilute conditions. This is likely because the nature of the PPI differ between the two conditions. Indeed, PPI are actually composed of many underlying interactions which vary differently according to the distance between interacting molecules (Table I) (23–25). Potentials which are short-ranged are typically proportional to the inverse of the sixth power of the distance between molecules. They are significant within 0.3–0.5 nm from a protein's surface and usually become negligible at 0.8–1.0 nm (26). The most common examples are the van der Waals attractions, which include

Table I. Underlying Interactions Comprising Protein-Protein Interactions [a]

Interaction Potential	Interaction Type at Minimum Energy State	Range Category	$W(r)$ [b]
Electrostatic Charge-Charge (incl. repulsive term of DLVO eqn.)	Repulsive	Long	$\propto r^{-1}$
Charge-Dipole	Attractive	Mid	$\propto r^{-4}$
Charge-Induced Dipole	Attractive	Mid	$\propto r^{-4}$
Dipole-Dipole [c]	Attractive	Short	$\propto r^{-6}$
Induced Dipole-Dipole [c]	Attractive	Short	$\propto r^{-6}$
Induced Dipole-Induced Dipole [c]	Attractive	Short	$\propto r^{-6}$
Aromatic Stacking	Attractive	Short	$\propto r^{-6}$
Hydrogen Bonding	Attractive	Short	$\propto r^{-10}$
Hard Sphere (Excluded Volume)	Repulsive	Short	∞ for $r \le (d+2\sigma)$ [d] 0 for $r > (d+2\sigma)$ [e]
Osmotic	Attractive	Short	
Hydrophobic	Attractive	Short	
Specific Ionic Interactions	Attractive	Short	

[a] references are in the text
[b] $W(r)$ is the potential as function of the distance r between interacting species
[c] van der Waals attractions
[d] d is the protein diameter; σ is the hydration layer thickness
[e] $W(r) = -\frac{4}{3}\pi d_{23}^3(\rho \cdot kT)\left[1 - \frac{3r}{4d_{23}} + \frac{r^3}{16d_{23}^3}\right]$ for $(d+2\sigma) \le r \le 2d_{23}$
$W(r) = 0$ for $r > 2d_{23}$
where d_{23}=(d + ion diameter +2σ)/2 and ρ=ion conc.

dipole-dipole, dipole-induced dipole, and induced dipole-induced dipole interactions. They are attractive because molecules in solution can align themselves to complement their dipoles. Other short-range interactions include hydrophobic interactions, hydrogen bonding, specific ionic attractions, hard sphere or excluded volume potential, and the osmotic attraction potential (24). In certain models of protein self-association, the first three, along with the van der Waals attractions, may be grouped under an associative potential (22,24). The potential assumes a square well form when a specific association site of one protein is within a certain distance of another such site on a second protein. The osmotic attraction potential arises from the exclusion of salt between closely contacting proteins (24). Thus, it is significant at high salt concentrations (> 100 mM ionic strength) and small inter-protein distances. Long-range potentials are proportional to the inverse of the distance between two proteins and can be significant even at distances of 1.5–2.0 nm (26). The most common example is electrostatic charge-charge repulsion governed by Coulomb's law. Mid-range interactions are simply a combination of the two. At low concentrations where the distances among molecules are large, only long-range interactions are expected to affect the overall PPI (22). However, as the concentration is increased and inter-protein distances decrease, the long-range interactions become stronger but the short-range interactions become significant (22). Their net effect determines the overall PPI. In fact, it is not uncommon for the different interactions to oppose each other (27).

In this study, we investigate the contributions of the various long- and short-range interactions to overall PPI in solutions of our model IgG_2 mAb at different pHs and at low and high concentrations. In particular, we focus on the roles of electrostatic charge-charge repulsions, dipole-dipole attractions, and specific region-region interactions. Expanding on the work of Saluja *et al*. (20,22), solutions of the mAb were further characterized over a wider pH range. High frequency rheology analyses, dynamic light scattering and circular dichroism studies, and zeta-potential measurements were performed. In addition, a 3D computer model of the mAb was created to study the distribution of its charges. Net charges, dipole moments, dipole orientations, and electrostatic potential surfaces at different pHs of the whole mAb and its Fc and Fab fragments were calculated in silico. From this data, the magnitudes of the long- and short-range interactions were quantitated in order to assess their specific contributions to mAb PPI in solution.

MATERIALS AND METHODS

Materials and Sample Preparation

The human IgG_2 monoclonal antibody analyzed was donated by Pfizer Biologics (St. Louis, MO, USA) and has a molecular weight of 144 kD. Its pI is 9.0 as determined by gel isoelectric focusing. All reagents were obtained from Fisher Scientific (Fair Lawn, NJ, USA). The buffer reagents are as follows: acetic acid-sodium acetate for pH 4.0 and 5.4, monobasic-dibasic sodium phosphate for pH 7.4, TRIS for pH 9.0, glycine for pH 10.0 and 11.0, and arginine for pH 12.0. To minimize the possibility that the different buffer species themselves, regardless of their effect on pH, can affect mAb solution behavior, buffers were prepared with low concentrations of the buffer salts and adjusted to the target ionic strength with sodium chloride. Specifically, buffers were prepared at concentrations of 1.0 mM or 10 mM with Milli-Q^{TM} grade water and adjusted to an ionic strength of 4 mM or 300 mM, respectively, with sodium chloride. They were then passed through 0.1 μm filters (Millipore, Billerica, MA, USA) to remove foreign particles. mAb solutions were prepared by multiple dialysis cycles against the selected buffer and were concentrated to greater than 120 mg/ml with Millipore Amicon Ultra centrifugation dialysis tubes. mAb concentration was determined by UV absorption with a Cary 50-Bio UV-Vis spectrophotometer (Varian Inc., Palo Alto, CA, USA). The extinction coefficient is 1.48 at 280 nm for a 0.1% mAb solution. The pH of the dialyzed solutions was observed and, if necessary, carefully adjusted to the target pH with sodium hydroxide or hydrochloric acid. The solutions were then diluted with their respective buffers to obtain the desired concentrations. We should note that the ionic strengths of the samples were not examined after dialysis. At low buffer ionic strength, the Donnan effect may cause the sample ionic strength to differ from 4 mM. Nevertheless, any such variation will still result in an ionic strength significantly less than the contrasting high ionic strength condition of 300 mM.

High Frequency Rheology Studies

The high frequency shear rheometer used in this study consists of a 10 MHz resonance frequency piezoelectric quartz crystal sandwiched between gold-plated electrodes (International Crystal Manufacturing Company, Oklahoma City, OK, USA) which are connected to a Hewlett Packard HP4194A impedance analyzer (Agilent Technologies, Palo Alto, CA, USA). The impedance analyzer subjects the crystal to an alternating current, causing it to vibrate according to the piezoelectric effect. Electrical properties including resistance, reactance, and impedance are obtained. By applying solution atop the crystal, changes in those values can then be used to determine the G' and G'' of the solution (18–20). $|\eta^*|$ is the square root of the sum of the squares of the two moduli divided by the resonance frequency (see online Supplementary Materials). Small quantities of mAb solutions (20 μl) from 20 to 120 mg/ml at different pHs and ionic strengths were analyzed at 25°C. All samples were analyzed in triplicate and the results averaged. More details regarding the development and use of the rheometer can be found in previous studies by our group (18–20,22).

Circular Dichroism Studies

mAb secondary and tertiary structure information at different pHs and ionic strengths were determined from far- and near-UV circular dichroism (CD) spectra, respectively, which were acquired with a Jasco 710 polarimeter (JASCO Inc., Easton, MD, USA). Far- and near-UV CD spectra were obtained from mAb solutions of 0.5 and 1.0 mg/ml, respectively. Each spectrum is the average of at least five scans each with a resolution of 0.5 nm collected at 20 nm per minute. Spectra of the buffers were also obtained and subtracted from

the spectra of protein samples in the corresponding buffer. The spectra were then normalized for concentration and the results reported in molar ellipticities (degrees·cm^2·dmol^{-1}).

Zeta Potential Measurements

Zeta potentials of 3.0 mg/ml mAb solutions at different pHs and 4 mM ionic strength were determined at 25°C by laser Doppler electrophoresis using a Zetasizer Nano ZS unit (Malvern Instruments Ltd., Worcestershire, UK). Zeta potentials were calculated from the mAb mean electrophoretic mobility, which is obtained by the method of Phase Analysis Light Scattering. All scans were performed in monomodal mode which involves fast electric field reversals to separate the effect of electro-osmosis from the movements of the proteins. All samples were analyzed in triplicate and the results averaged.

Dynamic Light Scattering

Dynamic light scattering (DLS) studies were performed on mAb solutions of 4.0, 8.0, and 12.0 mg/ml at different pHs and ionic strengths at 25°C with the same Zetasizer Nano ZS unit used to obtain zeta potentials. Prior to measurement, protein solutions were centrifuged with a mini-centrifuge to settle any dust particles. Measurements at pH 10.0 and 11.0 were performed in a glove bag under nitrogen gas to minimize any changes in pH due to atmospheric carbon dioxide. A total of 10 scans of 5 s each were recorded for each sample. All samples were analyzed in triplicate and the results averaged. Mutual diffusion coefficients were obtained and plotted as a function of concentration.

Computer Modeling

A 3D mAb computer model was constructed by modifying the X-ray crystallographic structure of an IgG2aκ murine mAb, mAb 231 (PDB ID: 1IGT), obtained from the RCSB Protein Data Bank (28,29). The molecular modeling programs Hyperchem Professional 7.5.1 (30) and Discovery Studio 2.1 (31) were used. The sugar units were first removed from the 1IGT Fc fragment. Next, the mAb amino acid sequence was compared with the 1IGT sequence to find the optimal homology match. 1IGT residues that differed were converted to those of the mAb with Hyperchem Professional's Mutate command, while insertions were performed with the Replace command. The side chains of pairs of cysteine residues in close proximity were then linked with disulfide bonds. Since the mAb is human-derived, its structure was configured such that four of the disulfide bonds are located within the hinge region (32). Next, the mAb hinge region adjacent to the Fab fragments was shortened by removing ten residues (5 per heavy chain) corresponding to a deletion between 1IGT and the mAb. This subsequently required positioning those fragments closer to the remaining hinge region in order to reestablish the bonds between them. Finally, in order to relieve any steric clashes among atoms, all sidechains, inserted residues, and residues within 6Å of deleted residues were subjected to minimization first by steepest descent until the gradient was less than 1.0 kcal·(Å·mol)$^{-1}$ followed by the calculation of the Polak-Ribiere conjugate gradient until it was less than 0.1 kcal·(Å·mol)$^{-1}$. Computer models of the Fc and Fab fragments were made by removing a portion of the hinge region. The "structural" hinge in human IgG1 encompasses residues 221–237 (32). This corresponds to the mAb sequence CCVECPPCPAPPVAGP. Its deletion results in the three fragments. The atomic coordinates of the mAb and its fragments were saved in the PDB format for further analysis.

The software PROPKA (33,34) was used to calculate the pKas of the ionizable residues. PROPKA utilizes a fast empirical approach that determines pKas based on the local environment of residues within the protein structure.

MAb and mAb fragment net charges were determined as a function of pH. The net charge is the sum of the charges of all ionizable residues. The charges of aspartic and glutamic acids, tyrosines, cysteines, and carboxyl termini were calculated with a modified Henderson-Hasselbalch equation that gives values between zero and −1:

$$\text{negative residue charge} = -\frac{10^{(\text{pH}-\text{pKa})}}{1+10^{(\text{pH}-\text{pKa})}} \quad (1)$$

Similarly, lysine, arginine, histidine, and amino termini charges are determined according to a similar equation that yields values between zero and +1:

$$\text{positive residue charge} = 1-\frac{10^{(\text{pH}-\text{pKa})}}{1+10^{(\text{pH}-\text{pKa})}} \quad (2)$$

Partial charges of individual atoms are required to determine the dipoles and electrostatic potential surfaces. Atomic radii are also needed for calculation of the potential surfaces. Most atomic partial charges and all atomic radii were obtained from the CHARMM 27 forcefield's topology file (35). However, atomic partial charges for neutral amino termini, neutral carboxyl termini, negatively charged cysteines, negatively charged tyrosines, and neutral arginines are not included. These were calculated with the program VCharge (36,37), which utilizes a fast algorithm to accurately reproduce partial charge values similar to those from quantum mechanical (Hartree-Fock 6-31G*) calculations, but independent of molecular conformation. To model proteins at a specific pH, ionizable residues are typically set in a fully ionized state with a ±1 charge or fully neutralized state with zero charge. Fractional charges are not considered. This is because an ionizable proton can only be shown as present or absent in a computer model. Therefore, the partial charges of atoms of an ionizable residue will sum to either zero or ±1. However, this approximation is not appropriate, especially when the pH is very close to an ionizable residue's pKa. In such situations, the residue's charge will be between zero and ±1. To address this, the Henderson-Hasselbalch equations were used to adjust the atomic partial charges based upon the user-defined pH. For example, the partial charge of an aspartic acid carboxyl oxygen is −0.55 when protonated and −0.76 when ionized. If the pH is equal to the residue's pKa, the partial charge will be −0.655.

The dipole of the mAb and its fragments is a vector given by

$$\text{dipole} = \sum_i q_i(\hat{r}_i - \hat{c}) \quad (3)$$

where q_i is the atomic partial charge of the ith atom, $\hat{r}_i$ contains the x, y, and z coordinates of the ith atom, and $\hat{c}$ is the center of mass vector which is determined according by

$$\hat{c} = \frac{\sum_i \mathrm{aw}_i \times \hat{r}_i}{\mathrm{MW}} \quad (4)$$

where aw_i is the atomic weight of the ith atom and MW is the protein molecular weight. Since the dipole of a charged protein can vary with the protein's location, the protein is centered about a reference point, commonly the center of mass (38). The dipole moment is simply the magnitude of the dipole and is equal to the square root of the sum of the squares of the dipole's x, y, and z values.

Electrostatic potential values were determined with the Adaptive Poisson Boltzmann Solver program (APBS) (39). The program requires PQR files with atomic coordinates and atomic partial charges of the mAb or its fragments. PQR files were generated from the PDB files by a program written in-house. APBS also requires an input file of user-defined parameters. Default parameter settings were obtained with the program PDB2PQR (40), which can generate APBS input files. Modified settings include the protein and solvent relative dielectric constants (4.0 and 78.54), the ion concentration (0.010 M), and the number of grid points (x=y=z=161).

Finally, the software VMD was used to create 3D graphical representations of the mAb, its dipoles, and electrostatic potential surfaces (41). In order to display the dipoles within the same scale as the proteins, the dipoles are reduced to 5% of their magnitude. In addition, since these computations required manipulating vast amounts of numerical data, scripts and programs were written in-house in the JAVA 1.4.2 programming language (42) to facilitate these operations.

RESULTS

High Frequency Rheology Studies

Rheological profiles of mAb solutions at different pHs and 4 mM or 300 mM ionic strength are shown in Fig. 1. Previous studies determined the profile from pH 4.0 to the pI of 9.0 (20,22) while solutions at pHs 10.0, 11.0, and 12.0 were also analyzed in this study. Due to solution shear thinning at high oscillating frequencies, the complex viscosities are lower than viscosities typically obtained with a gravitational-based capillary viscometer (6,23). Regarding studies performed at 4 mM ionic strength, a mAb concentration of 20 mg/ml has a negligible contribution to $|\eta^*|$ over the pH range. PPI as quantitated by G' are zero, and only G'' contributes to the viscosity. (As mentioned, G' is relatively insensitive at low concentrations.) G'' is almost exclusively due to the solvent, since the viscosity remains close to 1.0 cP, the value for water. As the concentration is increased, differences in $|\eta^*|$ *versus* pH become apparent. At 60 mg/ml, $|\eta^*|$ is still mainly due to G'' since G' remains near zero except at the extremes of the pH range. At 120 mg/ml, $|\eta^*|$ is still primarily due to G'', but differences in PPI *versus* pH become apparent as indicated by

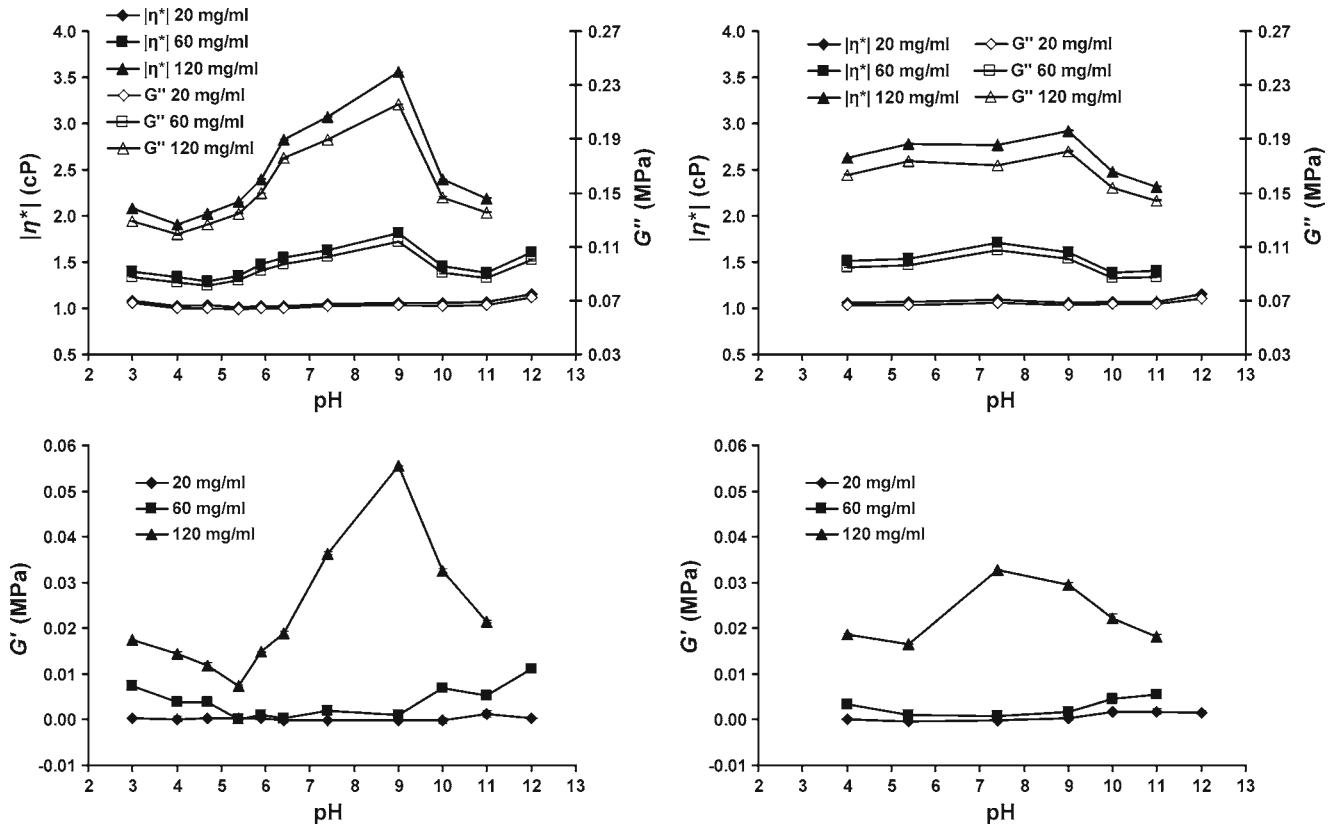

Fig. 1. Rheological properties as a function of pH at different mAb concentrations and ionic strengths. Left column: 4 mM ionic strength. Right column: 300 mM ionic strength. Note the scale difference between the G' and G'' y-axes. For all plots, error bars not visible are smaller than the symbol.

the G' *versus* pH trend. Also, all three rheological properties reach a maximum at the pI of 9.0 and decrease at pHs immediately surrounding it. Finally, an interesting phenomenon is seen around pH 4.0 to 5.4. At 120 mg/ml, $|\eta^*|$ and G'' are minimal at pH 4.0 while G' is minimal at pH 5.4. At 60 mg/ml, $|\eta^*|$ and G'' are minimal at pH 4.7, while G' is still minimal at pH 5.4. These properties increase immediately above and below those pHs. Studies at 300 mM ionic strength show that high salt concentrations reduce the variation in $|\eta^*|$, G', and G'' over the pH range (Fig. 1, right column). The curves begin to level, with lower values increasing and higher values decreasing. This is most apparent at 120 mg/ml.

Circular Dichroism Studies

Fig. 2 shows the far- and near-UV CD spectra at pHs 10.0, 11.0, and 12.0 and 4 mM and 300 mM ionic strength along with previously published results (20). The far UV-CD spectra show a strong negative band at 217 nm for all pHs and ionic strengths, indicating that the mAb is composed primarily of β-sheets. mAb secondary structure is constant at pHs 4.0, 9.0, 10.0, and 11.0. At pH 12.0 the spectra show broadening at 217 nm and a shift towards lower wavelengths, indicating secondary structure changes. Within the region of 260 to 300 nm of the near UV-CD spectra at both low and high ionic strengths, the most negative bands are seen at pH 9.0, indicating that the mAb is most compact at its pI. At pH 4.0, the spectra are only marginally less negative. At pHs 10.0 and 11.0, an apparent decrease in the intensity of the negative bands is observed, although the spectra fine structure is maintained. This indicates that the protein is slightly expanded under these conditions. The decrease in intensity is slightly greater at higher ionic strengths for pH 11.0. At pH 12.0, the spectra are highly positive and featureless, indicating a significant loss of tertiary structure. Interestingly, gelation of mAb solutions was observed at this pH above 100 mg/ml, but not at other pHs, perhaps due to the unfolding. Overall, the CD studies show that the mAb exists in a partially or completely unfolded state at pH 12.0. The protein is only slightly unfolded at pHs 10.0 and 11.0 and remains in the native state at pHs 4.0 to 9.0.

Zeta Potential Studies

Fig. 3 *A* shows the results of zeta potential measurements at different pHs and 4 mM ionic strength. Due to technique refinement, the results are more reliable than those from Saluja *et al.* (20). The mAb potential is most positive at pH 4.0 and decreases with increasing pH. From pH 4.0 to 9.0, the potential's decrease is fairly linear and crosses 0.0 mV at pH 7.5. Interestingly, this neutral point differs from the pI of 9.0. From pH 9.0 to 11.0, a much sharper decrease is observed, resulting in a zeta potential of −44.0 mV at pH 11.0 as compared to a potential of only +21.0 mV at pH 4.0.

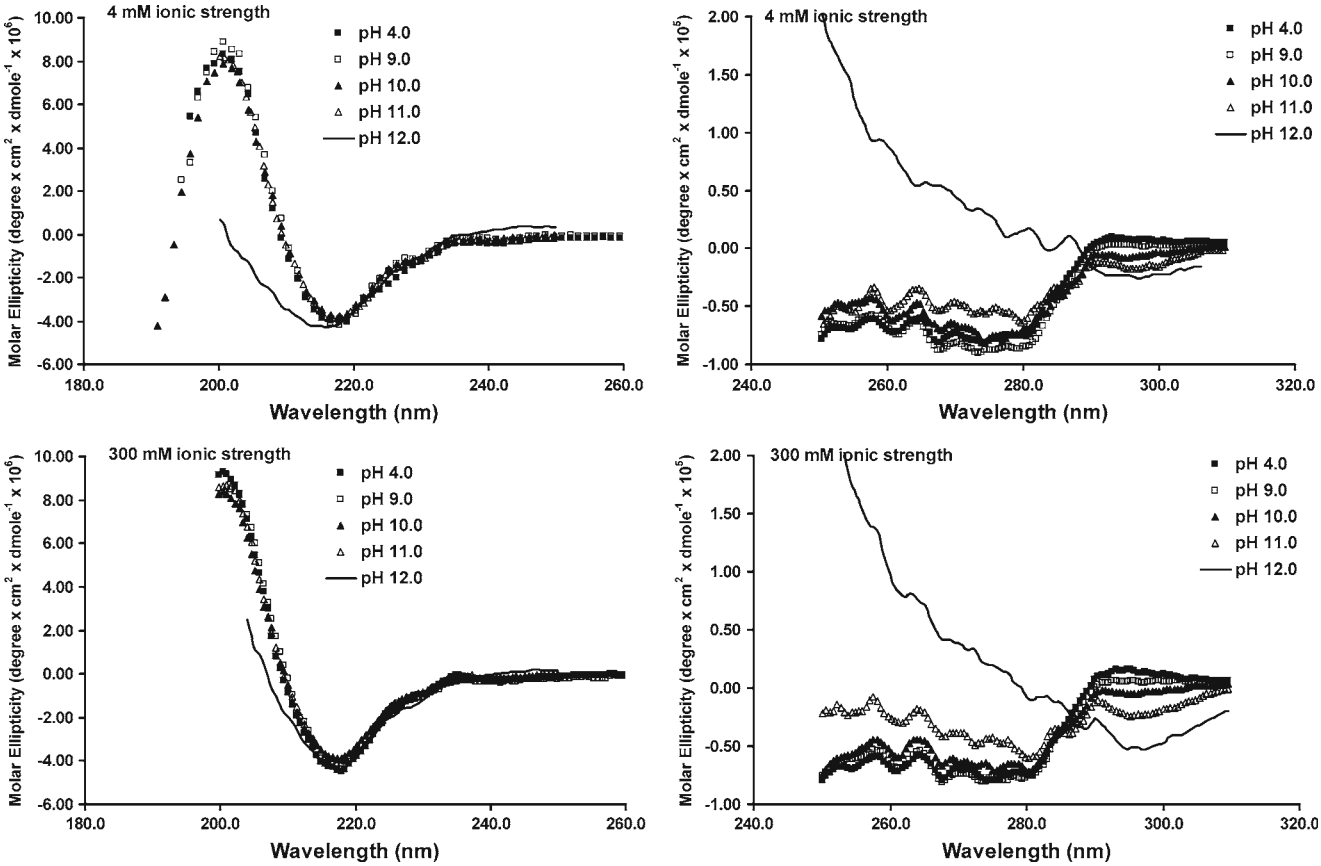

Fig. 2. Far-UV (left column) and near-UV (right column) CD spectra of mAb solutions at 4 and 300 mM ionic strength and different pHs. For all plots, error bars not visible are smaller than the symbol.

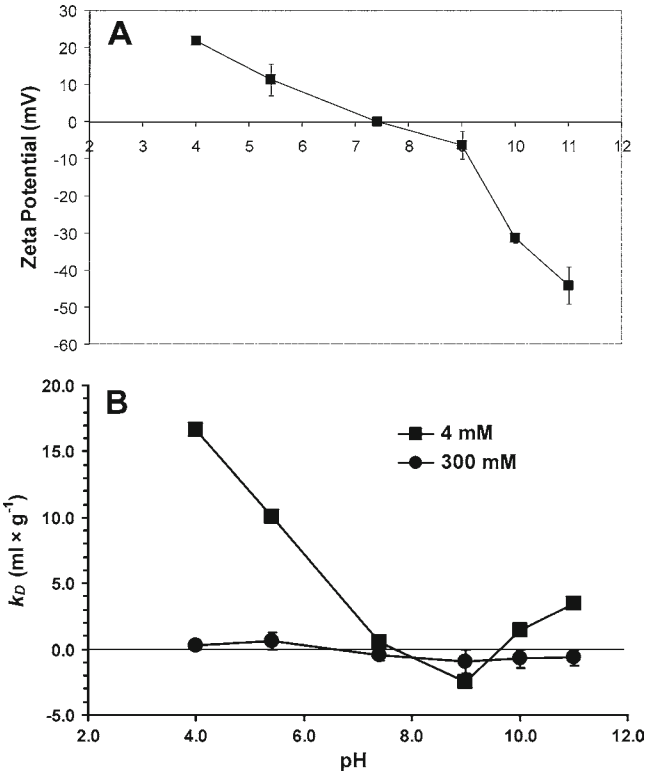

Fig. 3. (**A**) Zeta potentials of mAb solutions at 4 mM ionic strength and different pHs. (**B**) k_D *versus* pH from DLS measurements at 4 mM and 300 mM ionic strength. For all plots, error bars not visible are smaller than the symbol.

Dynamic Light Scattering Studies

In DLS, a solution is exposed to an incident light source, and the variation in intensity of the scattered light is measured over time (23). The fluctuations in intensity result from the random motion of solute molecules and are quantified by the experimentally determined mutual diffusion coefficient (D_m) (16). A more rapid change in intensity translates to greater D_m values and thus faster diffusion (16). Fig. 3 *B* shows the k_D values obtained from DLS studies conducted at pHs 10.0 and 11.0 and at 4 mM and 300 mM ionic strengths as well as previously reported results at other pHs (22). As mentioned, the interaction parameter k_D is a measure of PPI at low concentrations (16). A more positive k_D correlates with greater repulsive PPI while a more negative k_D correlates with greater attractive PPI (16,22). The k_D values were obtained by plotting D_m *versus* concentration (c) and fitting a regression line to the following equation (16):

$$D_m = D_0 + (k_D \times D_0)c \tag{5}$$

D_0 is the diffusion coefficient of an isolated solute molecule at infinite dilution, i.e. zero c. From pH 4.0 to 7.4 at 4 mM ionic strength, k_D decreases but remains positive, indicating that repulsive PPI are decreasing. At pH 7.4, k_D is close to zero with attractive and repulsive PPI balanced. At the pI of 9.0, k_D is negative and net PPI is attractive. From the pI to pH 11.0, k_D becomes positive and increases, meaning that PPI are repulsive again. At 300 mM ionic strength, charge screening by the salt ions results in k_D values close to zero at all pHs.

Computer Modeling: Calculated Net Charge and Dipole Moments

Fig. 4 *A* shows the calculated net charge as a function of pH for the mAb and its fragments. The calculated pI is 9.0, similar to the experimental pI, with values of 8.1 and 9.3 for the Fc and Fab fragments. Although the net charge of the mAb and its fragments decreases from pH 5.0 to 10.0, the drop is very gradual as compared to the change from pH 0.0 to 5.0 and pH 10.0 to 14.0. This profile is consistent with the mAb zeta potentials which decrease gradually from pH 4.0 to 9.0, then sharply from pH 9.0 to 11.0.

The calculated dipole moments of the mAb and its fragments *versus* pH are shown in Fig. 4 *B*. The maximum mAb dipole moment occurs at pH 2.0 and decreases rapidly as the pH is increased to 5.0. It then remains fairly level until pH 10.0, where it begins to rise rapidly to a peak at pH 12.0. However, the dipole moment at pH 12.0 is lower than at pH 2.0. Since an antibody is comprised of three loosely connected fragments subject to fluctuation, the mAb dipole moment is also expected to fluctuate. Therefore, it is also informative to examine the dipole moments of the fragments which are fairly rigid in contrast to the mAb as a whole (also refer to the 2nd and 4th row of Fig. 5). From pH 0.0, the Fc dipole moment peaks at pH 3.0 and decreases until about pH 5.0. From there, it steadily increases to its maximum value at pH 11.5

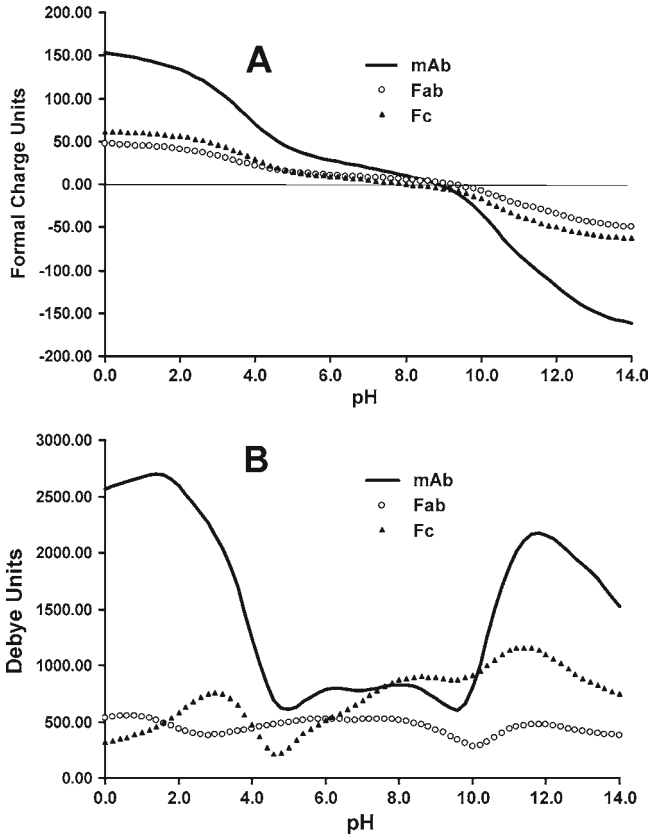

Fig. 4. (**A**) Calculated net charge vs. pH for the mAb and its fragments. (**B**) Calculated dipole moment vs. pH for the mAb and its fragments. Charges and dipole moments of the two Fabs have been averaged.

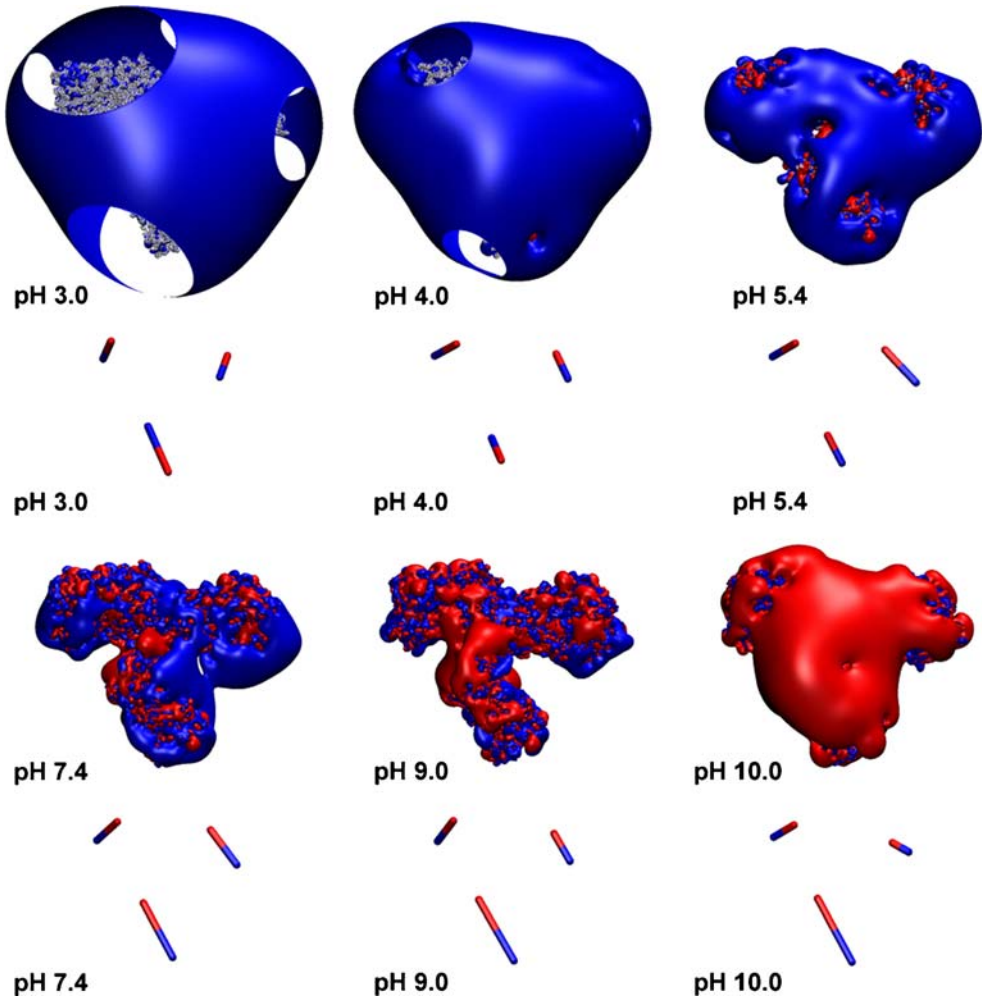

Fig. 5. Variation in the calculated electrostatic potential surfaces (first and third row) and dipoles of the Fab and Fc fragments (second and fourth row) with pH. Potential Surfaces: Red or blue contours in space indicate the −1 or +1 kT/e potential. White/gray surfaces indicate the mAb van der Waals surface. Dipoles: Positive ends are blue and negative ends are red.

whereupon it starts to decrease again. In contrast, the average Fab dipole moment increases gradually from pH 3.0 to 5.0 and stays level until pH 8.0. After this, it drops to its minimum level at pH 10.0 and then rises to a peak at pH 12.0.

Computer Modeling: Visualization of Dipole Moments, Dipole Orientations, and Electrostatic Potential Surfaces

Fig. 5 shows the Fab and Fc dipole orientations and the mAb electrostatic potential surfaces. Interestingly, the fragments' dipoles are oriented with the positive (blue) ends pointing outwards and the negative (red) ends pointing towards the center hinge region except for pHs 3.0 and 4.0 where the Fc dipole is oppositely oriented. This flip means that the Fc dipole no longer negates the net dipole of the Fab fragments. Not surprisingly, this corresponds to the dramatic increase in the mAb dipole moment from pH 5.0 to 2.0 as seen in Fig. 4 *B*. In contrast, the relatively low and constant mAb dipole moment from pH 5.0 to 10.0 is due to the fragments' dipoles canceling each other. Also notable is that the Fab dipoles have a mirror image orientation. In fact, this configuration is expected since the Fabs share the same amino acid sequence and are located on opposite sides of an axis of symmetry that bisects the Fc fragment. This may be an evolutionary design meant to keep an antibody's antigen recognition site open for binding. If Fabs within the same antibody approached each other, like two hands of a clock nearing midnight, the positive ends of their dipoles would repel each other.

The fragments' dipole orientations correspond to the development and change in the electrostatic potential surfaces. The red contour in space represents the location of the −1 kT/e potential surface, while the blue shows the location of the +1 kT/e surface. At the lowest pH, the abundance of blue and relative absence of red shows the effect due to the predominance of positive charges. As the pH increases, negative (red) surfaces start to develop and the amount of blue decreases. Red colors appear first in areas in which the negative ends of the dipoles reside. This is especially notable at the center hinge region. As the pH continues to increase, the negative potentials begin to dominate, and the positive (blue) potentials start to disappear. The blue colors disappear last in areas where the positive ends of the dipoles are

located. At the pI of 9.0, the red and blue surfaces are evenly distributed. It is interesting that significant dipoles can still exist at either high or low pHs where positive or negative charges predominate.

DISCUSSION

As mentioned earlier, characterizing PPI within highly concentrated protein solutions typically involves utilizing techniques that require low concentrations and then assuming the results are applicable at high concentrations. Because such assumptions may not be valid, we developed a high frequency shear rheometer for direct PPI analysis at high concentrations via the G' values. Nevertheless, those techniques—i.e. CD and DLS studies, zeta potential measurements, and computer modeling which can only process a single mAb model—can still yield information to explain the PPI quantitated by G'. This is because certain protein features such as net charge are independent of concentration. Also, such information obtained at low concentrations is essentially measures of long-range interactions.

Analysis of the rheology of highly concentrated mAb solutions (Fig. 1) showed that electrostatic charge-charge repulsions comprise a significant portion of the PPI. Such interactions are long-ranged (Table I) and are mitigated by the presence of salt. Indeed, the change in the rheological properties from 4 mM to 300 mM ionic strength at 120 mg/ml show the effect of charge screening due to salt. With contributions from electrostatics greatly reduced, the rheological properties show greater influence from protein volume and concentration, and therefore their variation *versus* pH is reduced. However, since their profiles are not entirely flat, non-electrostatic interactions, which have likely always been present, are now more apparent. This is observed from the PPI as quantitated by G' at high salt concentration. These residual interactions are likely short-range attractions since only electrostatic charge-charge repulsion is long-ranged (Table I). Thus, at high concentrations and low ionic strength, both long- and short-range interactions can contribute significantly to overall PPI. In fact, this is supported by the observation that the rheological properties are greatest at the pI at low ionic strength and decrease at the immediately surrounding pHs. At the pI, the mAb net charge is zero, and, therefore, charge-charge repulsions are minimal. This means their opposition of the short-range attractions is also minimal, which allows those interactions to have maximum effect, resulting in the highest $|\eta^*|$ and G'. Not surprisingly, for many other proteins, the phenomenon of minimum solubility occurs at the pI for the same reasons (43).

Before discussing the DLS results and their quantitation of PPI at low concentrations, one issue regarding the k_D values requires addressing. Previous studies have stated that k_D is composed of a thermodynamic term minus a hydrodynamic term (16):

$$k_D = 2B'_{22} - (\xi_1 + v_{sp}) \tag{6}$$

The thermodynamic term B'_{22} is the second osmotic virial coefficient of the solution multiplied by the solute's molecular weight. The latter two terms comprise the hydrodynamic term. v_{sp} is the partial specific volume of the solute, while ξ_1 is obtained from the virial expansion of the concentration-dependent frictional coefficient ξ (16):

$$\xi = \xi_0(1 + \xi_1 c + \ldots) \tag{7}$$

Thus, the concern arises as to how the hydrodynamic term affects interpretation of k_D with regard to PPI. For example, B'_{22} could be positive or zero, indicating repulsive or no net PPI, but subtraction of the hydrodynamic term may yield a negative k_D, thus suggesting attractive PPI. To address this, consider that B'_{22} is composed of a pairwise energetic interaction term (E_{B22}) and an excluded volume term (V_{B22}) (44). After variable substitution and grouping of the volume and frictional terms, k_D is given by

$$k_D = 2E_{B22} + (2V_{B22} - \xi_1 - v_{sp}) \tag{8}$$

From this equation and from the k_D values at high ionic strength, we can determine that the volume and frictional terms in the parenthesis sum to zero at the pHs studied and that k_D is due only to energetic mAb-mAb interactions. At 300 mM ionic strength, the k_D values are essentially zero, or are not significantly different from zero. This means that $2E_{B22}$ and ($2V_{B22}$ - ξ_1 - v_{sp}) sum to zero. Due to high salt and low mAb concentration, $2E_{B22}$, which is primarily due to electrostatic repulsions, is negligible. Therefore, ($2V_{B22}$ - ξ_1 - v_{sp}) must also be essentially zero. When the ionic strength is reduced, $2E_{B22}$ will become significant, but since the volume and frictional terms are not likely to be affected by salt, they will not change. Thus, k_D is strictly a function of E_{B22}, or the through-space energy of attraction or repulsion between mAbs.

With regard to dilute mAb solutions, only electrostatic interactions contribute significantly to PPI. This is supported by the k_D *versus* pH profile obtained from DLS studies (Fig. 3*B*). Increasing the ionic strength reduces the k_D values to zero at all pHs studied, indicating that the PPI are mainly electrostatic and thus shielded by salt. In addition, in contrast to the G' *versus* pH profile at 120 mg/ml and 4 mM ionic strength, PPI as quantitated by k_D are minimal at the pI. In the former case, PPI are greatest at the pI because although charge-charge repulsions are zero due to zero net charge, the effect of short-range attractions is still significant. These attractions may also be responsible for the G' reversal point at pH 5.4, which is absent in the k_D *versus* pH plot. However, at low concentrations where inter-protein distances are large, those interactions are very weak and do not influence k_D to a significant degree. This means that charge-charge repulsions almost fully constitute the PPI at low concentrations. Furthermore, this is supported by a plot of the absolute values of the calculated mAb net charge *versus* pH (Fig. 6*B*) which closely matches the k_D *versus* pH profile (Fig. 3*B*). (It is unclear why the absolute values of the zeta potentials in Fig. 3*A* do not correspond similarly to the k_D *versus* pH profile. They also do not follow the G' *versus* pH trend. Chloride ion binding may shift the zeta potential neutral point to pH 7.4 from the isoelectric pI of 9.0, yet it apparently does not affect the rheology or PPI which correspond more closely to the calculated net charge profile. Perhaps for this mAb, ion binding only affects zeta potential measurements. It should be noted, however, that a closer inspection of the k_D values at the pI show that the short-range interactions do have a

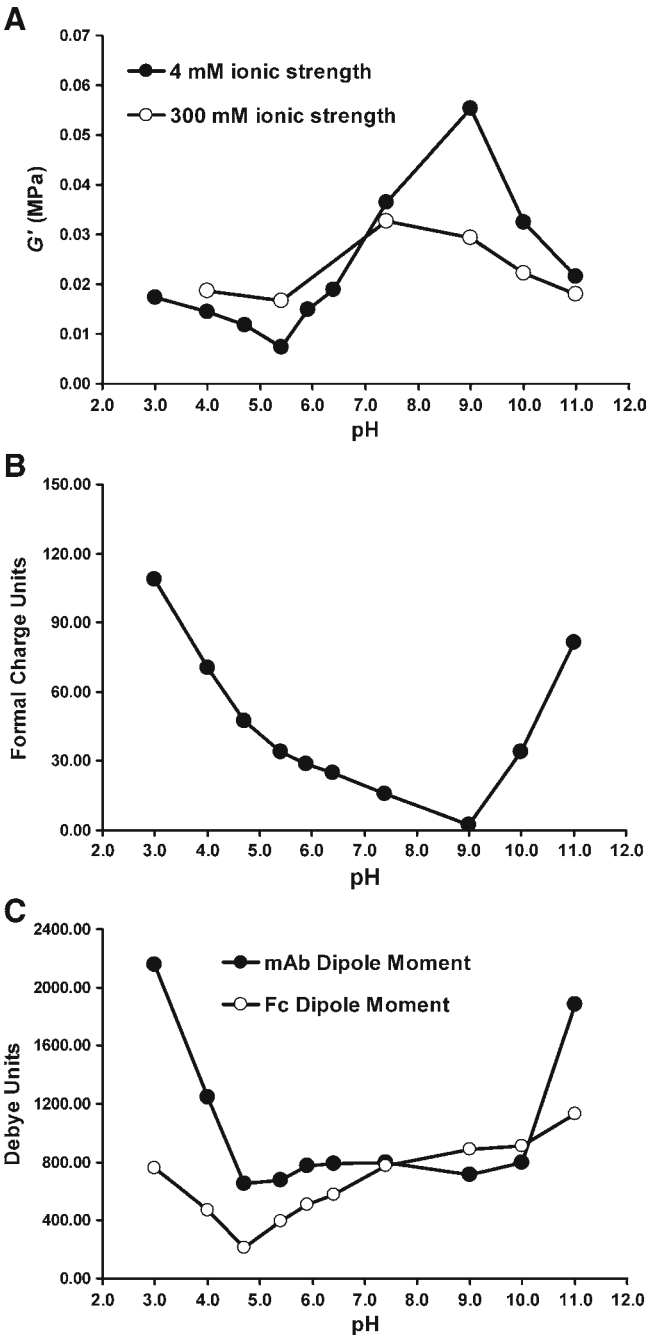

Fig. 6. Contributions of long-range repulsions and short-range attractions to PPI. (A) G' *versus* pH at 120 mg/ml. G' quantitates PPI. Error bars not visible are smaller than the symbol. (B) Absolute value of calculated mAb net charge *versus* pH. Net charge quantitates repulsion. (C) Dipole moment *versus* pH. Dipole moment quantitates attraction.

measurable effect, although miniscule, at low concentrations. At 4 mM ionic strength, the k_D is slightly negative, indicating slight attractions. At 300 mM ionic strength, those attractions are diminished, and k_D is not significantly different from zero. At pHs other than 9.0, the attractions are likely still present but are simply negated by the charge-charge repulsions.

Having established the nature and behavior of the long-range interactions, the additional contributions of the short-range interactions, especially at high concentrations, need to be discussed. Many of these interactions in Table I, such as induced dipole-induced dipole attractions, are difficult to quantify. Therefore, we will mainly focus on the contributions of dipole-dipole interactions while conceding that other short-range interactions may also be present to a significant degree. Fig. 6 shows, as a function of pH, (A) the G' values at 120 mg/ml and 4 mM or 300 mM ionic strength from Fig. 1, (B) the absolute values of calculated mAb net charges from Fig. 4*A*, and (C) calculated dipole moments from Fig. 4*B*. G' quantitates PPI, while the dipole moments and the absolute values of the net charges indicate the strength of short-range attractions and long-range electrostatic repulsions, respectively. From pH 4.7 to 9.0, the attractions (mAb dipole moment) remain constant while the repulsions (mAb net charge absolute value) decrease. Around pH 4.7 to 5.4, repulsions and attractions roughly cancel, and the G' is lowest at 4 mM ionic strength. As the pH increases, repulsions decrease, allowing the attractions to have a greater effect. At the pI of 9.0, the repulsion is zero, and only the short-range attraction is present. Thus, G' is highest here. At pH 3.0 and 4.0, repulsions are greatest, but the dipole moments are significantly greater than at other pHs. Therefore, the increase in G' from pH 5.4 to 3.0 is a result of attractions increasing at a greater rate than repulsions. From pH 9.0 to 10.0, attractions remain constant but repulsions increase, resulting in lower net attractions and a lower G'. From pH 10.0 to 11.0, the dipole moment increases considerably while repulsions also increase. Based on the observations at pH 3.0 and 4.0, the attraction from the larger dipole moment should greatly counter the increased repulsion, resulting in an increase in G'. Yet the G' decreases. This phenomenon may be due to the additional effect of mAb unfolding. CD studies established that the protein becomes increasingly unfolded from pH 10.0 to 12.0 but remains in the native state from pH 4.0 to 9.0 (Fig. 2). Nevertheless, it is encouraging to see that our modeling results correspond to the experimental G' values within the pharmaceutically relevant pH range of 4.0 to 8.0. The effect of higher ionic strength on G' can be explained by assuming that the attractions are shielded to a lesser

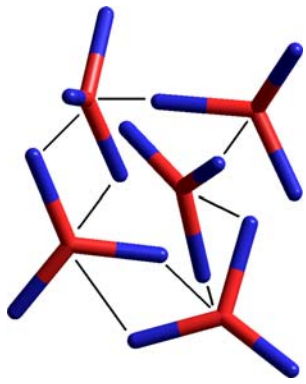

Fig. 7. Putative atomic view of mAb interactions in a highly concentrated solution at the pI. Based on the computer modeling results, the negative potentials are centered (red) and the positive potentials are peripheral (blue). Black lines indicate attractions between areas of positive and negative potential.

degree than the electrostatic repulsions. This is because the magnitude of van der Waals attractions due to dipole-dipole or dipole-induced dipole interactions are less affected by higher salt concentrations (45). Therefore, a significant reduction of the repulsions combined with a slight to moderate decrease in attractions, especially those below pH 4.7 and above pH 10.0, would result in less variation in PPI across the pH range. Indeed, the trend of *G′ versus* pH flattens from 4 mM to 300 mM ionic strength.

In assessing the contribution of long- and short-range interactions to PPI, we also considered each fragment's charge distribution. Fig. 6 *C* shows that the Fc dipole moment from pH 3.0 to 9.0 follows the trend of *G′ versus* pH at 120 mg/ml and 4 mM ionic strength (Fig. 6 *A*). This is not observed for the Fab dipole moments (Fig. 4 *B*), which suggests that short-range interactions due to the Fc fragment could be the main contributor to PPI at and below pH 9.0. Above pH 9.0, mAb unfolding, as mentioned in the previous paragraph, may also significantly influence PPI. In fact, if mAb charge-charge repulsions (Fig. 6 *B*) and attractions quantitated by the Fc dipole (Fig. 6 *C*) are summed, it would result in a net PPI trend even better resembling the *G′ versus* pH curve at 4 mM ionic strength below pH 10.0 (Fig. 6 *A*). Furthermore, the Fc dipole flips from pH 4.0 to 5.4 (Fig. 5), which corresponds to the reversal point in the *G′ versus* pH plot at 4 mM ionic strength. Based on these observations, one may argue that the short-range interactions should have been represented by the Fc dipole moment instead of that of the whole mAb. However, this ignores interactions due to the Fab fragments.

At this point, we cannot propose a definitive mechanism of how our mAbs interact at high concentrations. Although the calculated dipole moments of the mAb and Fc fragment both appear to be sufficient measures of short-range interactions below pH 10.0, the role of other such interactions need to be explored. For example, fluorescence studies with a hydrophobic probe have previously shown that the mAb's hydrophobicity is constant from pH 4.0 to 9.0. Hydrophobic attractions are very weak and are easily countered by electrostatic repulsions (27). Yet it might be significant at the pI where those repulsions are minimal or at pHs 10.0 to 12.0 where the mAb has a tendency to unfold. In addition, studies on different antibodies have determined that high viscosity originates from Fab-Fab interactions among the antibodies, resulting in a network at high concentrations (9). In contrast, our research suggests that both long- and short-range interactions are involved and that the Fc fragment may play a greater role than the Fabs in determining PPI and rheology for our mAb. In addition, based on the electrostatic potential surface distributions (Fig. 5), we propose that our mAb forms a slightly different network at its pI at high concentrations (Fig. 7). The network arises from dipole alignment among different fragments of different mAb molecules and from interactions among areas of positive and negative potential (pH 9.0 in Fig. 5).

CONCLUSIONS

In this study, we have shown that the PPI in solutions of our model mAb are based on contributions from long- and short-range interactions among the proteins. At high concentrations and low ionic strength, long-range electrostatic interactions in the form of charge-charge repulsions are present. Short-range interactions such as dipole-dipole attractions are also significant. In contrast, at low concentrations where inter-protein distance is large, only electrostatic repulsions are significant. Also, PPI at high concentrations may also originate from interactions between fragments of different mAb units which can lead to network formation.

These findings have two main implications for the formulation of highly concentrated protein therapeutics. First, when using techniques that require low sample concentrations to characterize formulations, we have shown that one should be cautious of assuming the results are similar at high concentrations because more types of interactions are significant at this condition. Therefore, direct characterization of high concentration formulations is desired when possible. The second implication involves the benefits of computer modeling for mAb design. The technique has the potential for predicting PPI at high concentrations, albeit after further refinement and rigorous validation. In this study, our mAb was modeled, and the net charges and dipole moments *versus* pH were calculated. The former corresponds to long-range repulsions while the latter to short-range attractions. The combination of these interactions correlated well with the experimentally determined *G′* values in the pharmaceutically relevant pH range of 4.0 to 8.0. Therefore, by modeling a therapeutic mAb, one can predict the effect of specific mutations on overall PPI. For example, one may find that mutating an aspartic acid to an asparagine in the Fc region may reduce the calculated mAb dipole moment. This would correspond to lower dipole-dipole attractions. Such mutations can be performed at locations away from the antigen recognition site in order to predict if PPI can be lowered without affecting mAb efficacy. Eventually, such predictions may result in new formulations with lower viscosity and/or a reduced potential for aggregation.

ACKNOWLEDGEMENTS

The authors thank Pfizer Inc. for donating the mAb for this study and for partial financial support of this work.

REFERENCES

1. Fulton AB. How crowded is the cytoplasm? Cell. 1982;30:345–7.
2. Zimmerman SB, Minton AP. Macromolecular crowding: biochemical, biophysical, and physiological consequences. Annu Rev Biophys Biomol Struct. 1993;22:7–65.
3. Minton AP. Influence of macromolecular crowding upon the stability and state of association of proteins: Predictions and observations. J Pharm Sci. 2005;94:1668–75.
4. Wang W, Singh S, Zeng DL, King K, Nema S. Antibody structure, instability, and formulation. J Pharm Sci. 2006;96:1–26.
5. Shire SJ, Shahrokh Z, Liu J. Challenges in the development of high protein concentration formulations. J Pharm Sci. 2004;2004:1390–402.
6. Liu J, Nguyen MD, Andya JD, Shire SJ. Reversible self-association increases the viscosity of a concentrated monoclonal antibody in aqueous solution. J Pharm Sci. 2005;94:1928–40.
7. Saluja A, Kalonia DS. Nature and consequences of protein-protein interactions in high protein concentration solutions. Int J Pharm. 2008;358:1–15.

8. Zhang J, Liu XY. Effect of protein–protein interactions on protein aggregation kinetics. J Chem Phys. 2003;119:10972–6.
9. Kanai S, Liu J, Patapoff TW, Shire SJ. Reversible self-association of a concentrated monoclonal antibody solution mediated by Fab-Fab interaction that impacts solution viscosity. J Pharm Sci. 2008;97:4219–27.
10. Meehan S, Berry Y, Luisi B, Dobson CM, Carver JA, MacPhee CE. Amyloid fibril formation by lens crystallin proteins and its implications for cataract formation. J Biol Chem. 2004;279:3413–9.
11. Harper JD, Lansbury PT. Models of amyloid seeding in Alzheimer's disease and scrapie: mechanistic truths and physiological consequences of the time-dependent solubility of amyloid proteins. Annu Rev Biochem. 1997;66:385–407.
12. Koo EH, Lansbury PT, Kelly JW. Amyloid diseases: abnormal protein aggregation in neurodegeneration. Proc Natl Acad Sci USA. 1999;96:9989–90.
13. Ganeval D, Noël LH, Preud'homme JL, Droz D, Grünfeld JP. Light-chain deposition disease: its relation with AL-type amyloidosis. Kidney Int. 1984;26:1–9.
14. Buxbaum JN, Chuba JV, Hellman GC, Solomon A, Gallo GR. Monoclonal immunoglobulin deposition disease: light chain and light and heavy chain deposition diseases and their relation to light chain amyloidosis. Clinical features, immunopathology, and molecular analysis. Ann Intern Med. 1990;112:455–64.
15. Zimm BH. Applications of the methods of molecular distribution to solutions of large molecules. J Chem Phys. 1946;14:164–79.
16. Teraoka I. Polymer solutions: an introduction to physical properties. New Jersey, USA: Wiley-IEEE; 2002.
17. George A, Chiang Y, Guo B, Arabshahi A, Cai Z, Wilson WW. Second virial coefficient as predictor in protein crystal growth. Methods Enzymol. 1997;276:100–10.
18. Saluja A, Kalonia DS. Measurement of fluid viscosity at microliter volumes using quartz impedance analysis. AAPS PharmSciTech. 2004;5:e47.
19. Saluja A, Kalonia DS. Application of ultrasonic shear rheometer to characterize rheological properties of high protein concentration solutions at microliter volume. J Pharm Sci. 2005;94:1161–8.
20. Saluja A, Badkar AV, Zeng DL, Nema S, Kalonia DS. Application of high-frequency rheology measurements for analyzing protein-protein interactions in high protein concentration solutions using a model monoclonal antibody (IgG2). J Pharm Sci. 2006;95:1967–83.
21. Hackley VA, Ferraris CF. Guide to rheological nomenclature for liquid-based particle systems. Maryland, USA: NIST; 2001.
22. Saluja A, Badkar AV, Zeng DL, Nema S, Kalonia DS. Ultrasonic storage modulus as a novel parameter for analyzing protein-protein interactions in high protein concentration solutions: correlation with static and dynamic light scattering measurements. Biophys J. 2007;92:234–44.
23. Hiemenz PC, Rajagopalan R. Principles of colloid and surface chemistry. New York, USA: Marcel Dekker; 1997.
24. Curtis RA, Prausnitz JM, Blanch HW. Protein-protein and protein-salt interactions in aqueous protein solutions containing concentrated electrolytes. Biotechnol Bioeng. 1998;57:11–21.
25. Elcock AH, McCammon JA. Calculation of weak protein-protein interactions: the pH dependence of the second virial coefficient. Biophys J. 2001;80:613–25.
26. Torshin IY. Bioinformatics in the post-genomic era: the role of biophysics. New York, USA: Nova Science; 2006.
27. Al-Shakhshira RH, Regnierb FE, Whitec JL, Hema SL. Contribution of electrostatic and hydrophobic interactions to the adsorption of proteins by aluminium-containing adjuvants. Vaccine. 1995;13:41–4.
28. Harris LJ, Larson SB, Hasel KW, McPherson A. Refined structure of an intact IgG2a monoclonal antibody. Biochem. 1997;36:1581–97.
29. RCSB Protein Data Bank. http://www.pdb.org (accessed December 2008).
30. Hyperchem Professional 7.5.1 (Hypercube, Inc., Gainesville, Florida, USA).
31. Discovery Studio 2.1 (Accelrys, Inc., San Diego, California, USA).
32. Nezlin R. The immunoglobulins: structure and function. London, UK: Academic; 1998.
33. Li H, Robertson AD, Jensen JH. Very fast empirical prediction and interpretation of protein pKa values. Proteins. 2005;61:704–21.
34. Bas DC, Rogers DM, Jensen JH. Very fast prediction and rationalization of pKa values for protein-ligand complexes. Proteins. 2008;73:765–83.
35. Brooks BR, Bruccoleri RE, Olafson BD, States DJ, Swaminathan S, Karplus M. CHARMM: a program for macromolecular energy, minimization, and dynamics calculations. J Comp Chem. 1983;4:187–17.
36. Gilson MK, Gilson HSR, Potter MJ. Fast assignment of accurate partial atomic charges. An electronegativity equalization method that accounts for alternate resonance forms. J Chem Inf Comput Sci. 2003;43:1982–97.
37. Chen W, Huang J, Gilson MK. Identification of symmetries in molecules and complexes. J Chem Inf Comput Sci. 2004;44:1301–13.
38. Felder CE, Prilusky J, Silman I, Sussman JL. A server and database for dipole moments of proteins. Nucleic Acids Res. 2007;35:W512–21.
39. Baker NA, Sept D, Joseph S, Holst MJ, McCammon JA. Electrostatics of nanosystems: Application to microtubules and the ribosome. Proc Natl Acad Sci USA. 2001;98:10037–41.
40. Dolinsky TJ, Nielsen JE, McCammon JA, Baker NA. PDB2PQR: an automated pipeline for the setup, execution, and analysis of Poisson-Boltzmann electrostatics calculations. Nuc Acids Res. 2004;32:W665–7.
41. Humphrey W, Dalke A, Schulten K. VMD—visual molecular dynamics. J Molec Graphics. 1996;14:33–8.
42. JAVA 1.4.2 programming language (Sun Microsystems, Inc., Santa Clara, California, USA).
43. Shaw KL, Grimsley GR, Yakovlev GI, Makarov AA, Pace CN. The effect of net charge on the solubility, activity, and stability of ribonuclease Sa. Protein Sci. 2001;10:1206–15.
44. Neal BL, Asthagiri D, Lenhoff AM. Molecular origins of osmotic second virial coefficients of proteins. Biophys J. 1998;75:2469–77.
45. Papp E, Fricsovszky G, Meszéna G. Electrodichroism of purple membrane. Biophys J. 1986;49:1089–100.